Tunable pseudo-magnetic fields for polaritons in strained metasurfaces

Charlie-Ray Mann,[1, *] Simon A. R. Horsley,[1] and Eros Mariani[1, †]

[1]*School of Physics and Astronomy, University of Exeter, Exeter, EX4 4QL, United Kingdom.*

Pseudo-magnetic fields generated in artificially strained lattices have enabled the emulation of exotic phenomena once thought to be exclusive to charged particles. However, to date, they have failed to emulate the tunability of real magnetic fields because they are determined solely by the engineered strain configuration, rendering them fixed by design. Here, we unveil a new universal mechanism to tune pseudo-magnetic fields for polaritons supported by a strained honeycomb metasurface composed of interacting dipole emitters/antennas. Without altering the strain configuration, we show that one can tune the pseudo-magnetic field strength by modifying the surrounding electromagnetic environment via an enclosing cavity waveguide, which modifies the nature of the dipole-dipole interactions. Remarkably, due to the competition between short-range Coulomb interactions and long-range photon-mediated interactions, the pseudo-magnetic field can be entirely switched off at a critical cavity width, without removing the strain. Consequently, by varying only the cavity width, we demonstrate a tunable Lorentz-like force that can be switched on/off and a collapse and revival of polariton Landau levels. Unlocking this tunable pseudo-magnetism poses new intriguing questions beyond the paradigm of conventional tight-binding physics.

Unfortunately, neutral particles do not directly couple to the electromagnetic gauge potentials. Therefore, exotic phenomena exhibited by charged particles in magnetic fields, such as the Lorentz force, Aharonov-Bohm effect, and Landau quantization, remain elusive for neutral particles. This fundamental limitation has inspired various ways of engineering artificial magnetic fields which are revolutionizing our ability to manipulate neutral particles [1–18]. Within graphene physics, it has been demonstrated that non-uniform strain can generate pseudo-magnetic fields which can mimic some of the properties of real ones [19–23]. This tantalizing concept has recently been emulated for photons by judiciously engineering aperiodicity in honeycomb photonic lattices of evanescently coupled waveguides, which mimic the tight-binding physics of graphene [12]. However, these emergent pseudo-magnetic fields in artificially strained lattices have failed to emulate one key property of real magnetic fields: tunability. While real magnetic fields that are applied across samples in the lab can be tuned by varying external parameters (e.g., the current through a solenoid), these pseudo-magnetic fields are determined solely by the engineered strain configuration, rendering them fixed by design. Most notably, it is impossible to switch the pseudo-magnetic field on/off after the photonic structure has been fabricated. Therefore, a fundamental question arises: how do we overcome this seemingly intrinsic lack of tunability?

Here we unveil a new universal mechanism to tune pseudo-magnetic fields for polaritons that requires no change to the strain configuration. In particular, we consider polaritons supported by a strained honeycomb metasurface composed of interacting electric dipole emitters/antennas. In addition to short-range Coulomb interactions between the dipoles, the dipoles also couple to the transverse photonic field which results in long-range dipole-dipole interactions mediated by

photons; crucially, both of these dipole-dipole interactions depend qualitatively on the surrounding electromagnetic environment in which the dipoles are embedded. Therefore, previous results derived from conventional tight-binding models do not trivially extend to lattices of interacting dipoles [24]. By exploiting this key difference we show that one can tune the artificial magnetic field by modifying the real electromagnetic environment.

To demonstrate this tunability we embed the metasurface inside a cavity waveguide where, by reducing the cavity width, one can modify the dominant dipolar coupling from Coulomb interactions to photon-mediated interactions. As a result, we unveil that one can tune the strength of the pseudo-magnetic field after the metasurface has been fabricated with a fixed strain configuration by varying a single external parameter: the cavity width. In fact, we reveal that one can even switch off the pseudo-magnetic field entirely at a critical cavity width, without removing the strain — this highly non-trivial result is impossible to achieve with photonic systems that emulate the tight-binding physics of graphene [25–27]. Consequently, we demonstrate a tunable Lorentz-like force that can be switched on/off, deflecting polariton wavepackets into effective cyclotron orbits whose radius can be controlled via the cavity width. For large strains, we also demonstrate Landau quantization of the polariton cyclotron orbits, where progressively decreasing the cavity width can induce a collapse and revival of the polariton Landau levels. This work reveals that rich physics emerges from non-trivial long-range interactions, and therefore poses many intriguing questions beyond the realm of conventional tight-binding models which can be explored in a variety of different experimental set-ups across the electromagnetic spectrum.

Minimal metasurface model.— A schematic of the cavity-embedded metasurface is depicted in figure 1a. We model the resonant electric dipoles with a generic bare polarizability $\alpha_0(\omega) = 2\omega_0\Omega(\omega_0^2 - \omega^2 - i\omega\gamma_{nr})^{-1}$ that is applicable to both classical antennas and quantum emitters in their linear regime, where Ω characterizes the strength of the polarizabil-
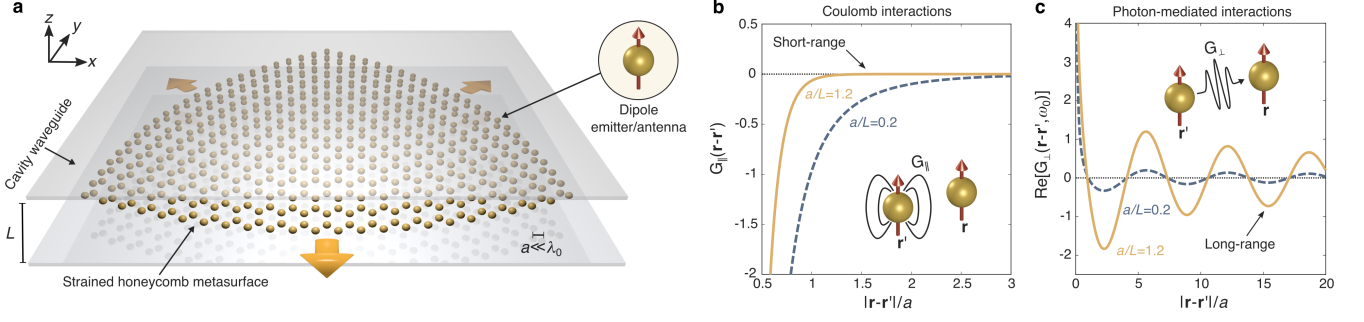
FIG. 1. **Cavity-tunable dipole-dipole interactions.** **a**, Schematic of a strained honeycomb metasurface composed of interacting dipole emitters/antennas embedded inside a cavity waveguide of width L, where the induced dipole moments point in the z-direction. We assume a subwavelength nearest-neighbour separation $a \ll \lambda_0$ such that the metasurface supports subradiant polaritons that are evanescently bound to the lattice. **b**, Longitudinal Green's function ($\mathsf{G}_\parallel$) for a large (dashed blue line) and small (solid orange line) cavity width, which mediates short-range Coulomb interactions. **c**, Real part of the transverse Green's function ($\mathsf{G}_\perp$) for a large (dashed blue line) and small (solid orange line) cavity width, which describes long-range coherent interactions mediated by the cavity photons. By varying the cavity width, one can tune the relative dominance between the Coulomb and photon-mediated interactions. Plots obtained with $\lambda_0 = 6.5a$.

ity, γ_{nr} accounts for non-radiative losses, and ω_0 is the free-space resonant frequency. We assume the polarizability to be anisotropic such that the induced electric dipole moments point in the z-direction (see inset). The unstrained metasurface is composed of a honeycomb array of dipoles which consists of two inequivalent hexagonal sublattices. Furthermore, we consider subwavelength nearest-neighbour separation $a \ll \lambda_0$, where λ_0 is the free-space resonant wavelength, so that the metasurface supports subradiant polaritons that are evanescently bound to the lattice. The strained metasurface is considered to have a fixed strain configuration where the dipoles are displaced according to a slowly-varying displacement field $\mathbf{u}(\mathbf{r}) = [u_x(\mathbf{r}), u_y(\mathbf{r})]$. Finally, the metasurface is embedded at the centre of a cavity waveguide of width L, where the cavity walls are assumed to be perfectly reflecting mirrors.

The interactions between the dipoles are mediated by the cavity Green's function $\mathsf{G}(\mathbf{r} - \mathbf{r}', \omega)$ which describes the field generated at $\mathbf{r}$ due to a point dipole source at $\mathbf{r}'$, and it can be decomposed into its longitudinal and transverse components $\mathsf{G}(\mathbf{r} - \mathbf{r}', \omega) = \mathsf{G}_\parallel(\mathbf{r} - \mathbf{r}') + \mathsf{G}_\perp(\mathbf{r} - \mathbf{r}', \omega)$ (see Methods for the full expressions and Supplementary Section 1 for the derivations). The longitudinal Green's function decays like

$$\mathsf{G}_\parallel(\mathbf{r} - \mathbf{r}') \sim \frac{\mathrm{e}^{-2\pi|\mathbf{r} - \mathbf{r}'|/L}}{\sqrt{|\mathbf{r} - \mathbf{r}'|}}, \tag{1}$$

and describes short-range Coulomb interactions whose strength decreases rapidly with the separation distance between dipoles as shown in figure 1b. In stark contrast, the transverse Green's function decays like

$$\mathsf{G}_\perp(\mathbf{r} - \mathbf{r}', \omega_0) \sim \frac{\mathrm{e}^{\mathrm{i}2\pi|\mathbf{r} - \mathbf{r}'|/\lambda_0}}{\sqrt{|\mathbf{r} - \mathbf{r}'|}}, \tag{2}$$

where the real part describes coherent long-range interactions mediated by the cavity photons whose strength oscillates and

decreases slowly with the separation distance as shown in figure 1c. This non-trivial nature of the photon-mediated interactions means that the metasurface is not amenable to a simple tight-binding model — in fact, we must include all the photon-mediated interactions between all pairs of dipoles to accurately describe the physics. Crucially, by varying the cavity width one can tune the relative dominance between these two distinct types of interactions; for large cavity widths ($L \sim \lambda_0$) the physics near the K/K$'$ points is dominated by the Coulomb interactions (see dashed blue lines in figures 1b-c), while for small cavity widths ($L \ll \lambda_0$) the Coulomb interactions are exponentially suppressed and the photon-mediated interactions become dominant (see solid orange lines in figures 1b-c).

Cavity-tunable pseudo-gauge potentials.— To gain analytical insight, we have used a coupled-dipole model to derive an effective Hamiltonian describing the polaritons near the K/K$'$ points, which is valid to leading order in the strain tensor $\varepsilon_{ij}(\mathbf{r}) = (\partial u_j/\partial r_i + \partial u_i/\partial r_j)/2$. For the K valley, the effective Hamiltonian reads ($\hbar = 1$)

$$\mathcal{H}_{\mathrm{K}} = \omega_{\mathrm{D}}(L)\mathbb{1} + \mathrm{i}v_{\mathrm{D}}(L)\boldsymbol{\sigma} \cdot \nabla + \Phi(\mathbf{r}, L)\mathbb{1} + \boldsymbol{\sigma} \cdot \mathbf{A}(\mathbf{r}, L), \tag{3}$$

where $\mathbb{1}$ is the identity matrix and $\boldsymbol{\sigma} = [\sigma_x, \sigma_y]$ is the vector of Pauli matrices acting in the sublattice space (see Methods for the derivation and equivalent Hamiltonian for the K$'$ valley). Therefore, the polaritons behave like massless Dirac quasiparticles with a linear Dirac cone dispersion [24], where $\omega_{\mathrm{D}}(L)$ is the Dirac frequency and $v_{\mathrm{D}}(L)$ is the Dirac velocity (see Methods for the expressions). As schematically shown in figure 2a, the strain leads to a spatially-varying shift of the Dirac cones in frequency and momentum which is effectively described by a pseudo-scalar potential $\Phi(\mathbf{r}, L) = \Phi_0(L)[\varepsilon_{xx}(\mathbf{r}) + \varepsilon_{yy}(\mathbf{r})]$ and a pseudo-vector potential $\mathbf{A}(\mathbf{r}, L) = A_0(L)[\varepsilon_{xx}(\mathbf{r}) - \varepsilon_{yy}(\mathbf{r}), -2\varepsilon_{xy}(\mathbf{r})]$, respectively. In figures 2b-c we show how the strain-independent parameters $\Phi_0(L)$ and $A_0(L)$ can be tuned by varying only
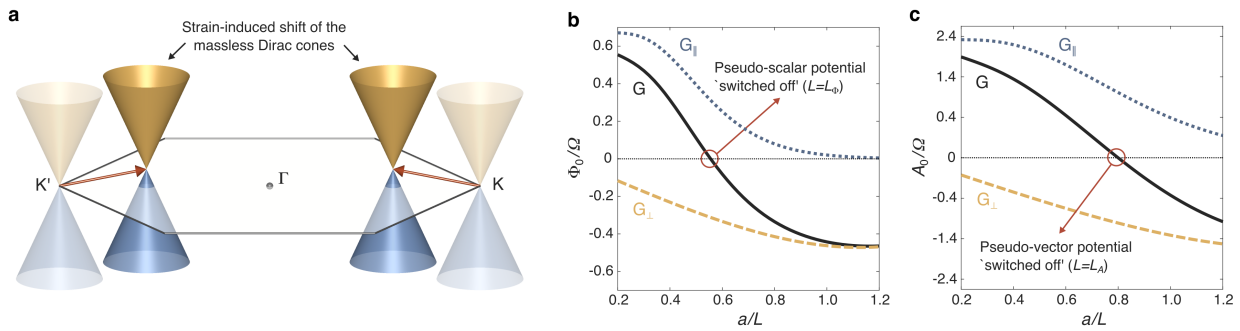
FIG. 2. **Cavity-tunable pseudo-gauge potentials. a**, The unstrained metasurface supports massless Dirac polaritons characterized by linear Dirac cones near the high symmetry K/K′ points. Applying strain leads to a shift of the Dirac cones in frequency and momentum which is effectively described by a pseudo-scalar and pseudo-vector potential, respectively. **b-c**, Show how the strain-independent parameters in the pseudo-scalar potential (Φ_0) and pseudo-vector potential (A_0) can be tuned by varying the cavity width (black solid lines), respectively. We also show the separate contributions emerging from the Coulomb interactions (blue dotted lines) and the photon-mediated interactions (orange dashed lines) which are always finite but have opposite signs. At critical cavity widths (L_Φ and L_A) these contributions cancel resulting in the pseudo-gauge potentials being switched off for any strain configuration. Plots obtained with $\lambda_0 = 6.5a$ and $\Omega = 0.01\omega_0$.

the cavity width (see Methods for the expressions). Remarkably, there exists critical cavity widths (L_Φ and L_A) where these parameters vanish identically, thereby switching off the pseudo-gauge potentials entirely for any strain configuration.

We stress that this is a highly non-trivial phenomenon. To switch off the pseudo-vector (scalar) potential one requires that the strain-induced change in the dipole locations within the metasurface does not change the intersublattice (intrasublattice) interaction energy. Within a nearest-neighbour tight-binding model, this would require one to engineer a hopping parameter that does not vary with distance; this is impossible to achieve with photonic analogs of graphene where the strength of the evanescent coupling strictly decreases with separation distance [25–27]. In general, the strain does change the interaction energy between any pair of dipoles in the metasurface; however, the sum of all these changes can be made to vanish. Crucially, while the contributions from the short-range Coulomb interactions and long-range photon-mediated interactions are always finite and never vanish individually, they have opposite signs and thus tend to compensate each other in the pseudo-gauge potentials (see dotted and dashed lines, respectively, in figures 2b-c). At the critical cavity widths, these contributions perfectly cancel making the pseudo-gauge potentials vanish. This ability to switch off and tune the pseudo-gauge potentials without modifying the strain opens up new perspectives beyond previously studied tight-binding models.

In what follows, we investigate some of the implications of the tunable pseudo-vector potential. Specifically, we consider a strain configuration described by the displacement field $\mathbf{u}(\mathbf{r}) = (\Delta/a)[2xy, x^2 - y^2]$ [12, 19], where Δ is a measure of the strain magnitude. This trigonal strain configuration gives rise to a vanishing pseudo-scalar potential $\Phi = 0$ and a spatially-varying pseudo-vector potential $\mathbf{A} = 4(\Delta/a)A_0[y, -x]$, leading to a uniform pseudo-magnetic field $\mathbf{B}_\tau = \tau \nabla \times \mathbf{A} = -\tau 8(\Delta/a)A_0\hat{\mathbf{z}}$ which, by

virtue of time-reversal symmetry, has opposite signs for the K ($\tau = +1$) and K′ ($\tau = -1$) valleys.

Cavity-tunable Lorentz-like force.— In the 'semiclassical' limit [28], polariton wavepackets propagating through the strained metasurface behave as if they were subjected to a Lorentz-like force $\mathbf{F}_\tau(L) = \text{sgn}(v_D)\hat{\mathbf{v}} \times \mathbf{B}_\tau$ which acts perpendicular to the group velocity direction $\hat{\mathbf{v}}$. Consequently, the polaritons exhibit cyclotron motion, as schematically depicted in figure 3a, in direct analogy with charged particles in real magnetic fields. Crucially, by modifying the nature of the dipole-dipole interactions via the cavity width, one can tune the magnitude of the Lorentz-like force and the effective cyclotron mass of the Dirac polaritons $m_c(L) = \delta\omega/v_D^2$, where $\delta\omega = \omega - \omega_D$ is the frequency relative to the Dirac point. As a result, in figure 3b we show how the corresponding cyclotron radius $R_c(L) = |m_c||v_D^2|/|\mathbf{F}_\tau|$ can be tuned by varying only the cavity width. The dotted line indicates the region of cavity widths where the linear approximation of the Dirac cone breaks down [24] (see Supplementary Section 2).

To verify the tunability of the cyclotron orbits, we simulated the evolution of Gaussian wavepackets using the effective Hamiltonian (3), and in figure 3c we plot the trajectories of their centre-of-mass for a metasurface with a fixed strain configuration, but different cavity widths (see Methods). As expected, the polariton wavepackets in the K/K′ valleys undergo cyclotron motion in opposite directions due to time-reversal symmetry (e.g., see snapshots along trajectory 6), and the orbit radii agree very well with the analytical predictions (see crosses in figure 3b). Note, the direction of the orbits depend on the signs of the Dirac velocity, cyclotron mass, and pseudo-magnetic field. For subcritical cavity widths $L > L_A$ where the short-range Coulomb interactions are dominant, the cyclotron radius expands as the cavity width is reduced (see trajectories 1-3). At the critical cavity width $L = L_A$, the pseudo-magnetic field is switched off and the polariton wavepackets feel no Lorentz-like force; they
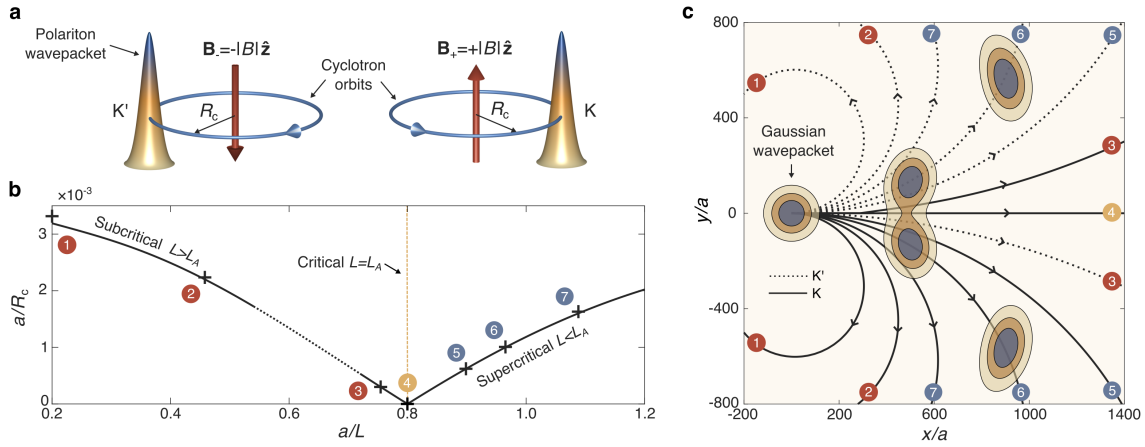
FIG. 3. **Cavity-tunable Lorentz-like force and cyclotron orbits. a**, Schematic of the cyclotron motion exhibited by polariton wavepackets due to a Lorentz-like force generated by a pseudo-magnetic field which has opposite signs in the K/K′ valleys. **b**, Predicted evolution of the cyclotron radius as the cavity width is reduced for a fixed strain configuration at a fixed frequency relative to the Dirac point (black line). **c**, Simulated trajectories of polariton wavepackets in the K/K′ valleys (solid/dashed lines) propagating through a strained metasurface with different cavity widths (calculated radii given by crosses in **b**). For subcritical cavity widths $L > L_A$, the cyclotron radius expands as the cavity width is reduced (trajectories 1-3). At the critical cavity width $L = L_A$, the wavepackets feel no Lorentz-like force (trajectory 4). For supercritical cavity widths $L < L_A$, the cyclotron orbits reemerge and the cyclotron radius shrinks as the cavity width is reduced further (trajectories 5-7). Plots obtained with $\Delta = 2 \times 10^{-5}$, $\delta\omega = -0.001\omega_0$, $\lambda_0 = 6.5a$, and $\Omega = 0.01\omega_0$.

propagate through the strained metasurface as if there was no strain present at all (see trajectory 4). For supercritical cavity widths $L < L_A$ where the long-range photon-mediated interactions become dominant, the cyclotron orbits reemerge and the cyclotron radius now shrinks as the cavity width is reduced further (see trajectories 5-7).

Cavity-tunable Landau levels.— For larger strains the pseudo-magnetic field increases and one can reach the 'quantum' limit, where the polariton cyclotron orbits undergo Landau quantization in direct analogy with charged particles in real magnetic fields [29]. Therefore, as schematically depicted in figure 4a, the massless Dirac cones collapse into a quantized Landau level spectrum $\omega_n(L) = \omega_D(L) + \mathrm{sgn}(n)\omega_c(L)\sqrt{|n|}$, where $n = 0, \pm 1, \pm 2 \ldots$ is the Landau level index, and $\omega_c(L) = \sqrt{2|v_D||\mathbf{B}_\tau|}$ is the effective cyclotron frequency. The polariton Landau levels have a characteristic squareroot dependence on the Landau level index and the strain magnitude, which is a manifestation of the pseudo-relativistic nature of the massless Dirac polaritons (see Supplementary Section 3).

In the previously studied photonic analog of graphene, the Landau level spectrum was fixed by the engineered strain configuration — to modify the pseudo-magnetic field they had to fabricate an entirely new structure with a different strain pattern [12]. In stark contrast, here we show that for a metasurface with a fixed strain configuration, the polariton Landau level spectrum depends qualitatively on the surrounding electromagnetic environment which mediates the dipole-dipole interactions. In fact, as shown in figure 4b, one can drastically reconfigure the Landau level spectrum by varying only the cavity width. As before, the dotted line indicates the region of cavity widths where the linear Dirac cone approximation

breaks down [24] (see Supplementary Section 4). Remarkably, the transition of the dominant dipolar coupling from Coulomb to photon-mediated interactions as the cavity width is reduced results in a collapse and revival of the polariton Landau levels, despite the metasurface having a fixed strain configuration.

To verify the tunability of the polariton Landau levels, we go beyond the approximations of the effective Hamiltonian and calculate the effective polarizability $\alpha_{\mathrm{eff}}(\omega)$ of a resonant dipole, which fully accounts for the strong multiple scattering within the metasurface (see Methods). From this, we define a local spectral function $\mathrm{Im}[\alpha_{\mathrm{eff}}(\omega)]$ which is related to the local density of states and characterizes the full spectral response of the metasurface. In figures 4c-e we show the local spectral function at the centre of a metasurface with a fixed strain configuration but different cavity widths, and the insets show the corresponding unstrained case.

For subcritical cavity widths $L > L_A$ where the short-range Coulomb interactions are dominant (see figure 4c), a sequence of resonant peaks emerge within the vicinity of the Dirac region where the effective Hamiltonian is valid. These peaks directly correspond to the predicted polariton Landau levels which are not present in the unstrained case. Note the spectral function has an asymmetry about the Dirac point due to long-range interactions between dipoles residing on the same sublattice which break the chiral symmetry. For example, more Landau levels can be observed above the Dirac point than below as the Dirac approximation holds for a wider frequency range. As the cavity width is reduced, the spacing between the Landau level peaks decreases in accordance with the analytical prediction (see Supplementary Section 4). At the critical cavity width $L = L_A$ (see figure 4d), the pseudo-
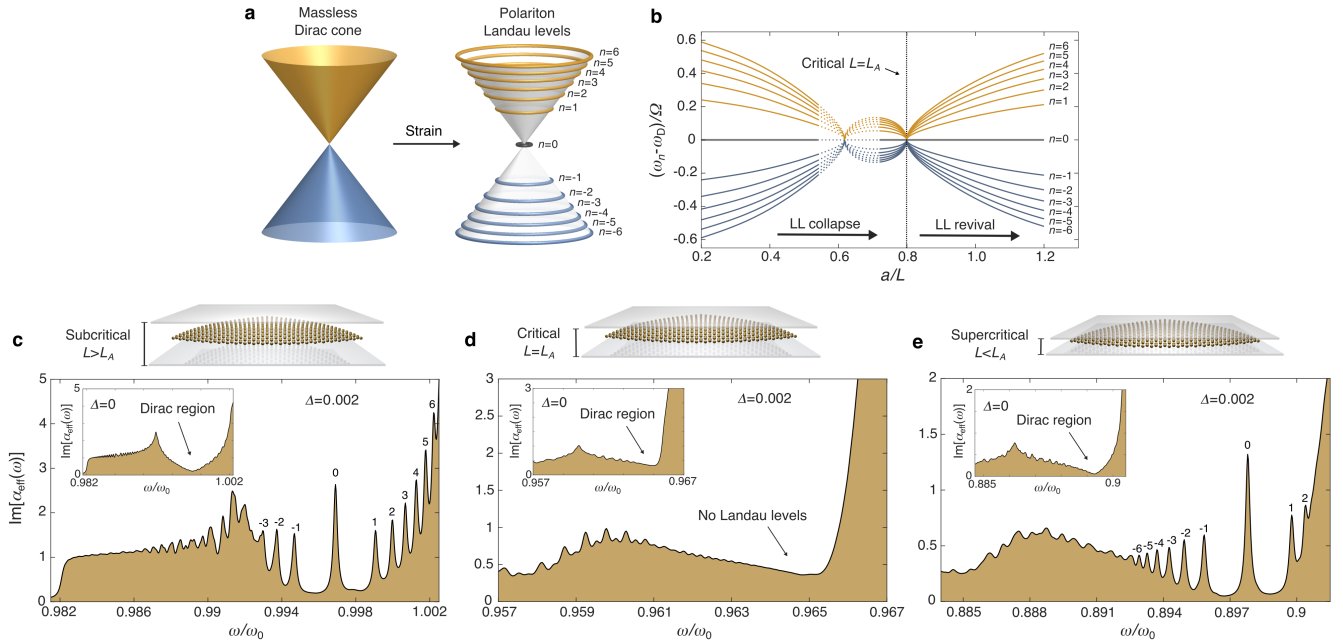
FIG. 4. **Cavity-induced collapse and revival of polariton Landau levels. a**, Schematic of a massless Dirac cone splitting into quantized polariton Landau levels. **b**, Predicted evolution of the Landau levels as the cavity width is reduced. **c-e**, Local spectral function at the centre of a metasurface with a fixed strain configuration, but different cavity widths of $a/L = 0.2$, $a/L = 0.83$, and $a/L = 1.2$, respectively (insets show the corresponding unstrained case). For subcritical cavity widths $L > L_A$ (see **c**), we observe Landau level peaks which are not present in the unstrained case (labelled according to their Landau index). At the critical cavity width $L = L_A$ (see **d**), the pseudo-magnetic field is switched off and therefore no Landau level peaks are observed. For supercritical cavity widths $L < L_A$ (see **e**), the Landau level peaks reemerge, thus verifying the collapse and revival of the polariton Landau levels. Plots obtained with $\Delta = 0.002$, $\lambda_0 = 6.5a$, $\Omega = 0.01\omega_0$, and $\gamma_{\rm nr} = 0.025\Omega$.

magnetic field is switched off and therefore the Landau levels completely vanish within the Dirac region, thus verifying the cavity-induced collapse of the polariton Landau levels. As the cavity width is reduced beyond this critical value, the Landau level peaks begin to reemerge (see Supplementary Section 4). For supercritical cavity widths $L < L_A$ where the long-range photon-mediated interactions become dominant (see figure 4e), a clear sequence of Landau level peaks can be observed within the Dirac region which are not present in the unstrained case, thus verifying the remarkable revival of the polariton Landau levels.

Experimental considerations.— Since the localized Landau level states are subradiant (see Supplementary Section 5), the width of the Landau level peaks is limited only by non-radiative losses. Therefore, to clearly resolve the Landau levels one must ensure that the Landau level spacing is larger than the non-radiative losses in the metasurface $\omega_{\rm c} \gg \gamma_{\rm nr}$.

We note that the general principle underlying this mechanism for tuning pseudo-magnetic fields can be generalized to include metasurfaces composed of classical antennas that exhibit magnetic dipole and higher order multipole moments, such as split-ring resonators and dielectric Mie resonators. To provide a concrete example of a possible classical realization which is well described by our minimal model, in Supplementary Section 6 we present finite-element simulations of a microwave metasurface composed of metallic he-

lical dipole antennas. Since metals behave approximately as perfect conductors at microwave frequencies the Landau level peaks should have a high quality factor. We have simulated the dispersion for unstrained and strained lattices to extract the effective Hamiltonian parameters as a function of the cavity width. Crucially, we show that there indeed exist critical cavity widths where the pseudo-gauge potentials vanish, in direct accordance with our analytical predictions. Using a vector network analyzer, one can map the entire Landau level spectrum in a single measurement by measuring the return loss of a near-field source antenna, which is related to the local density of states. Furthermore, one can also map the field distribution of the Landau level states using a second detector antenna which can be scanned across the metasurface [17].

Furthermore, our classical analysis is a valid description for a subwavelength array of quantum two-level emitters in the single-excitation subspace [30]. It would therefore be very interesting to explore these tunable pseudo-magnetic fields in the quantum regime, by considering subwavelength arrays of excitonic particles [31, 32] or atomic (atom-like) quantum emitters which have been attracting considerable interest in recent years [33–38]. Finally, we stress that there are many ways to modify the nature of the interactions between emitters/antennas by engineering different electromagnetic environments; for example, one could consider interactions mediated by surface plasmons in graphene [39] or guided modes

of photonic crystals [37, 40] which may provide alternative mechanisms to tune the pseudo-magnetic field.

Outlook.— This new universal mechanism for tuning pseudo-magnetic fields poses new intriguing questions beyond the realm of conventional tight-binding models. For example, do quantum-Hall-like edge states associated with the polariton Landau levels exist in the presence of long-range interactions? Can one controllably switch them on/off, or tune their properties, by modifying the nature of the dipole-dipole interactions? Moreover, do novel edge states emerge at interfaces separating regions with different electromagnetic environments? The polariton Landau levels also provide a novel way of sculpting the local density of states — this could be exploited for enhancing/suppressing light-matter interactions for emitters embedded in subwavelength photonic structures. Furthermore, while we have demonstrated a tunable Lorentz-like force and tunable Landau levels, one should also be able to observe Aharonov-Bohm-like interference patterns which will depend qualitatively on the surrounding electromagnetic environment. Finally, here we have focused on some of the implications of a tunable pseudo-magnetic field, but what are the implications of a tunable pseudo-electric field arising from the pseudo-scalar potential? To conclude, while intense efforts are devoted towards designing systems that emulate tight-binding models, this work hints towards a richer landscape of physics emerging from non-trivial long-range interactions which are prevalent in electromagnetic systems.

---

[1] Hafezi, M., Demler, E. A., Lukin, M. D. & Taylor, J. M. Robust optical delay lines with topological protection. *Nat. Phys.* **7**, 907-912 (2011).

[2] Umucalılar, R. O. & Carusotto, I. Artificial gauge field for photons in coupled cavity arrays. *Phys. Rev. A* **84**, 043804 (2011).

[3] Fang, K., Yu, Z. & Fan, S. Photonic Aharonov-Bohm effect based on dynamic modulation. *Phys. Rev. Lett.* **108**, 153901 (2012).

[4] Fang, K., Yu, Z. & Fan, S. Realizing effective magnetic field for photons by controlling the phase of dynamic modulation. *Nat. Photon.* **6**, 782-787 (2012).

[5] Fang, K. & Fan, S. Controlling the flow of light using the inhomogeneous effective gauge field that emerges from dynamic modulation. *Phys. Rev. Lett.* **111**, 203901 (2013).

[6] Hafezi, M., Mittal, S., Fan, J., Migdall, A. & Taylor, J. M. Imaging topological edge states in silicon photonics. *Nat. Photon.* **7**, 1001-1005 (2013).

[7] Lin, Q. & Fan, S. Light guiding by effective gauge field for photons. *Phys. Rev. X* **4**, 031031 (2014).

[8] Tzuang, L. D., Fang, K., Nussenzveig, P., Fan, S. & Lipson, M. Non-reciprocal phase shift induced by an effective magnetic flux for light. *Nat. Photon.* **8**, 701-705 (2014).

[9] Liu, F. & Li, J. Gauge field optics with anisotropic media. *Phys. Rev. Lett.* **114**, 103902 (2015).

[10] Schine, N., Ryou, A., Gromov, A., Sommer, A. & Simon, J. Synthetic Landau levels for photons. *Nature* **534**, 671-675 (2016).

[11] Schomerus, H. & Halpern, N. Y. Parity anomaly and Landau-level lasing in strained photonic honeycomb lattices. *Phys. Rev.*

Lett. **110**, 013903 (2013).

[12] Rechtsman, M. C. et al. Strain-induced pseudo-magnetic field and photonic Landau levels in dielectric structures. *Nat. Photon.* **7**, 153-158 (2013).

[13] Abbaszadeh, H., Souslov, A., Paulose, J., Schomerus, H. & Vitelli, V. Sonic Landau levels and synthetic gauge fields in mechanical metamaterials. *Phys. Rev. Lett.* **119**, 195502 (2017).

[14] Brendel, C., Peano, V., Painter, O. J. & Marquardt, F. Pseudo-magnetic fields for sound at the nanoscale. *Proc. Natl. Acad. Sci. U.S.A.* **114**, 3390-3395 (2017).

[15] Yang, Z., Gao, F., Yang, Y., & Baile, Z. Strain-induced gauge field and Landau levels in acoustic structures. *Phys. Rev. Lett.* **118**, 194301 (2017).

[16] Wen, X. et al. Acoustic Landau quantization and quantum-Hall-like edge states. *Nat. Phys.* **15**, 352-356 (2019).

[17] Jia, H. et al. Observation of chiral zero mode in inhomogeneous three-dimensional Weyl metamaterials. *Science* **363**, 6423 (2019).

[18] Peri, V., Serra-Garcia, M., Ilan, R. & Huber, S. D. Axial-field-induced chiral channels in an acoustic Weyl system. *Nat. Phys.* **15**, 357-361 (2019).

[19] Guinea, F., Katsnelson, M. I. & Geim, A. K. Energy gaps and a zero-field quantum Hall effect in graphene by strain engineering. *Nat. Phys.* **6**, 30-33 (2009).

[20] Levy, N. et al. Strain-induced pseudo-magnetic fields greater than 300 Tesla in graphene nanobubbles. *Science* **329**, 544-547 (2010).

[21] Low, T. & Guinea, F. Strain-induced pseudo-magnetic field for novel graphene electronics. *Nano Lett.* **10**, 3551-3554 (2010).

[22] Chaves, A., Covaci, L., Rakhimov, K. U., Farias, G. A. & Peeters, F. M. Wave-packet dynamics and valley filter in strained graphene. *Phys. Rev. B* **82**, 205430 (2010).

[23] de Juan, F., Cortijo, A., Vozmediano, M. A. H. & Cano, A. Aharonov-Bohm interferences from local deformations in graphene. *Nat. Phys.* **7**, 810-815 (2011).

[24] Mann, C.-R., Sturges, T. J., Weick, G., Barnes, W. L. & Mariani, E. Manipulating type-I and type-II Dirac polaritons in cavity-embedded honeycomb metasurfaces. *Nat. Commun.* **9**, 2194 (2018).

[25] Plotnik, Y. et al. Observation of unconventional edge states in 'photonic graphene'. *Nat. Mater.* **13**, 57-62 (2014).

[26] Bellec, M., Kuhl, U., Montambaux, G. & Mortessagne, F. Tight-binding couplings in microwave artificial graphene. *Phys. Rev. B* **88**, 115437 (2013).

[27] Jacqmin, T. et al. Direct observation of Dirac cones and a flat-band in a honeycomb lattice for polaritons. *Phys. Rev. Lett.* **112**, 116402 (2014).

[28] Ashcroft, N. W. & Mermin, N. D. *Solid State Physics* (Brooks Cole, Belmont, 1976).

[29] Landau, L. Diamagnetismus der metalle. *Z. Physik* **64**, 629-637 (1930).

[30] Svidzinsky, A. A., Chang, J.-T. & Scully, M. O. Cooperative spontaneous emission of N atoms: Many-body eigenstates, the effect of virtual Lamb shift processes and analogy with radiation of N classical oscillators. *Phys. Rev. A* **81**, 053821 (2010).

[31] Yuen-Zhou, J., Saikin, S. S., Yao, N. Y. & Aspuru-Guzik, A. Topologically protected excitons in porphyrin thin films. *Nat. Mater.* **13**, 1026-1032 (2014).

[32] Yuen-Zhou, J. et al. Plexciton Dirac points and topological modes. *Nat. Commun.* **7,** 11783 (2016).

[33] Bettles, R. J., Gardiner, S. A. & Adams, C. S. Enhanced optical cross section via collective coupling of atomic dipoles in a 2D array. *Phys. Rev. Lett.* **116**, 103602 (2016).

[34] Shahmoon, E., Wild, D. S., Lukin, M. D. & Yelin, S. F. Co-

operative resonances in light scattering from two-dimensional atomic arrays. *Phys. Rev. Lett.* **118**, 113601 (2017).

[35] Bettles, R. J. et al. Topological properties of a dense atomic lattice gas. *Phys. Rev. A* **96**, 041603 (2017).

[36] Perczel, J. et al. Topological quantum optics in two-dimensional atomic arrays. *Phys. Rev. Lett.* **119**, 023603 (2017).

[37] González-Tudela, A., Hung, C.-L., Chang, D. E., Cirac, J. I. & Kimble, H. J. Subwavelength vacuum lattices and atom-atom interactions in two-dimensional photonic crystals. *Nat. Photon.* **9**, 320-325 (2015).

[38] Bekenstein, R. et al. Quantum metasurfaces with atom arrays. *Nat. Phys.* **16**, 676-681 (2020).

[39] Nikitin, A. Y., Guinea, F., García-Vidal, F. J. & Martín-Moreno, L. Fields radiated by a nanoemitter in a graphene sheet. *Phys. Rev. B* **84**, 195446 (2011).

[40] Perczel, J., Borregaard, J., Chang, D. E., Yelin, S. F. & Lukin, M. D. Topological quantum optics using atom-like emitter arrays coupled to photonic crystals. *Phys. Rev. Lett.* **124**, 083603 (2020).

METHODS

The unstrained metasurface is composed of a honeycomb array of dipoles located at periodic positions $\mathbf{R}_A = \mathbf{R} - \mathbf{d}/2$ and $\mathbf{R}_B = \mathbf{R} + \mathbf{d}/2$ which form the A and B hexagonal sublattices, respectively. Here, $\mathbf{d} = a[0, 1]$ is the vector connecting the A and B sites in the unit cell, and $\mathbf{R} = l_1\mathbf{a}_1 + l_2\mathbf{a}_2$ are the set of lattice vectors, where l_1 and l_2 are integers, and $\mathbf{a}_1 = (\sqrt{3}a/2)[-1, \sqrt{3}]$ and $\mathbf{a}_2 = (\sqrt{3}a/2)[1, \sqrt{3}]$ are the primitive lattice vectors. The corresponding reciprocal lattice vectors are $\mathbf{G} = n_1\mathbf{b}_1 + n_2\mathbf{b}_2$, where n_1 and n_2 are integers, and $\mathbf{b}_1 = (2\pi/3a)[-\sqrt{3}, 1]$ and $\mathbf{b}_2 = (2\pi/3a)[\sqrt{3}, 1]$ are the primitive reciprocal lattice vectors. To describe an artificially strained metasurface we introduce a slowly-varying displacement field $\mathbf{u}(\mathbf{r})$, where the dipoles are located at new displaced positions $\bar{\mathbf{R}}_{A/B} = \mathbf{R}_{A/B} + \mathbf{u}(\mathbf{R}_{A/B})$. Finally, the metasurface is embedded at the centre of a cavity waveguide formed by two perfectly reflecting mirrors located at $z = \pm L/2$.

Effective polariton Hamiltonian.— To describe a resonant dipole's response to an external field, one has to modify the bare polarizability to take into account the interaction with its own scattered field. The renormalized polarizability of a resonant dipole inside the cavity reads

$$\alpha^{-1}(\omega) = \alpha_0^{-1}(\omega) - \Sigma(\omega), \tag{4}$$

where the polarizability correction is given by

$$\Sigma(\omega) = \mathrm{i}\frac{2a^3 k_\omega^3}{3} + \frac{4a^3}{L^3}\left[\mathrm{Li}_3\left(\mathrm{e}^{\mathrm{i}k_\omega L}\right) - \mathrm{i}k_\omega L\,\mathrm{Li}_2\left(\mathrm{e}^{\mathrm{i}k_\omega L}\right)\right], \tag{5}$$

where $k_\omega = \omega/c$ and $\mathrm{Li}_n(z) = \sum_{l=1}^{\infty} z^l/l^n$ is the polylogarithm of order n (see Supplementary Section 1 for the derivation). The first term in equation (5) is the usual radiative-reaction correction in free-space, whereas the other terms encode the corrections due to the cavity. In the absence of a driving field, the induced electric dipole moments $\mathbf{p}_{\mathbf{R}_A} = p_{\mathbf{R}_A}\hat{\mathbf{z}}$ and $\mathbf{p}_{\mathbf{R}_B} = p_{\mathbf{R}_B}\hat{\mathbf{z}}$ on the A and B sublattices are given by the self-consistent coupled-dipole equations

$$\frac{1}{\alpha(\omega)}p_{\mathbf{R}_A}(\omega) = \sum_{\mathbf{R}_A' \neq \mathbf{R}_A}\mathsf{G}(\bar{\mathbf{R}}_A - \bar{\mathbf{R}}_A', \omega)p_{\mathbf{R}_A'}(\omega) + \sum_{\mathbf{R}_B}\mathsf{G}(\bar{\mathbf{R}}_A - \bar{\mathbf{R}}_B, \omega)p_{\mathbf{R}_B}(\omega) \tag{6}$$

and

$$\frac{1}{\alpha(\omega)}p_{\mathbf{R}_B}(\omega) = \sum_{\mathbf{R}_B' \neq \mathbf{R}_B}\mathsf{G}(\bar{\mathbf{R}}_B - \bar{\mathbf{R}}_B', \omega)p_{\mathbf{R}_B'}(\omega) + \sum_{\mathbf{R}_A}\mathsf{G}(\bar{\mathbf{R}}_B - \bar{\mathbf{R}}_A, \omega)p_{\mathbf{R}_A}(\omega), \tag{7}$$

where the first/second sum in each equation corresponds to the field (z-component) generated by all the other dipoles belonging to the same/opposite sublattice (see Supplementary Section 1 for the derivation).

The interactions between the dipoles are mediated by the cavity Green's function which can be expressed in the spectral domain as

$$\mathsf{G}(\mathbf{r} - \mathbf{r}', \omega) = \mathrm{i}\frac{\pi a^3 k_\omega^2}{L}\sum_{m=-\infty}^{\infty}\left(1 - \frac{k_m^2}{k_\omega^2}\right)\mathrm{H}_0^{(1)}\left(|\mathbf{r} - \mathbf{r}'|\sqrt{k_\omega^2 - k_m^2}\right), \tag{8}$$

where $k_m = 2m\pi/L$ and $\mathrm{H}_0^{(1)}$ is the Hankel function of zeroth order and first kind (see Supplementary Section 1 for the derivation). We decompose the cavity Green's function (8) into its longitudinal and transverse components $\mathsf{G}(\mathbf{r} - \mathbf{r}', \omega) = \mathsf{G}_\parallel(\mathbf{r} - \mathbf{r}') + \mathsf{G}_\perp(\mathbf{r} - \mathbf{r}', \omega)$, where the longitudinal component can be expressed in the spectral domain as

$$\mathsf{G}_\parallel(\mathbf{r} - \mathbf{r}') = -\frac{4a^3}{L}\sum_{m=1}^{\infty}k_m^2\,\mathrm{K}_0\left(k_m|\mathbf{r} - \mathbf{r}'|\right), \tag{9}$$

where K_0 is the modified Bessel function of zeroth order and second kind (see Supplementary Section 1 for the derivation). Note, the longitudinal component is equivalent to equation (8) in the static limit $\omega \to 0$, and therefore mediates Coulomb interactions between the dipoles inside the cavity. In contrast, the transverse component $\mathsf{G}_\perp(\mathbf{r} - \mathbf{r}', \omega) = \mathsf{G}(\mathbf{r} - \mathbf{r}', \omega) - \mathsf{G}_\parallel(\mathbf{r} - \mathbf{r}')$ describes interactions that are mediated by the transverse photonic modes of the cavity. For simplicity, we retain only the dominant contribution from the fundamental transverse electromagnetic (TEM) mode of the cavity which has a linear dispersion $\omega_{\mathbf{k}} = c|\mathbf{k}|$ and polarization (along z-direction) that are independent of the cavity width. This is a good approximation since we are interested in the regime of cavity widths $L < \lambda_0$, where the higher order quantized cavity modes do not contribute to the long-range interactions between the dipoles. The corresponding Green's function for the TEM mode reads

$$\mathsf{G}_\perp^{\mathrm{TEM}}(\mathbf{r} - \mathbf{r}', \omega) = \frac{\mathrm{i}\pi a^3 k_\omega^2}{L}\mathrm{H}_0^{(1)}\left(k_\omega|\mathbf{r} - \mathbf{r}'|\right), \tag{10}$$

which is equivalent to the $m = 0$ term in equation (8) (see Supplementary Section 1 for the derivation).

In what follows, we derive the effective Hamiltonian for the K valley since the effective Hamiltonian for the K′ valley is related via time-reversal symmetry. To analyze the polaritons near the K point, we write the dipole moments as

$$p_{\mathbf{R}_A}(\omega) = \mathrm{e}^{\mathrm{i}\mathbf{K}\cdot\mathbf{R}_A}\psi_A^K(\mathbf{R}_A, \omega) \quad , \quad p_{\mathbf{R}_B}(\omega) = \mathrm{e}^{\mathrm{i}\mathbf{K}\cdot\mathbf{R}_B}\psi_B^K(\mathbf{R}_B, \omega), \tag{11}$$

where ψ_A^K and ψ_B^K are slowly-varying envelope fields for the A and B sublattices, respectively. To not overburden notation we suppress the valley index until the end. By introducing the Fourier transform of the envelope fields

$$\widetilde{\psi}_A(\mathbf{k}, \omega) = \int\frac{\mathrm{d}^2\mathbf{r}}{2\pi}\psi_A(\mathbf{r}, \omega)\mathrm{e}^{-\mathrm{i}\mathbf{k}\cdot\mathbf{r}}, \quad \widetilde{\psi}_B(\mathbf{k}, \omega) = \int\frac{\mathrm{d}^2\mathbf{r}}{2\pi}\psi_B(\mathbf{r}, \omega)\mathrm{e}^{-\mathrm{i}\mathbf{k}\cdot\mathbf{r}} \tag{12}$$

we can write the coupled-dipole equations in matrix form as

$$\frac{1}{\check{\alpha}(\omega)}\widetilde{\psi}(\mathbf{k}, \omega) = \int\mathrm{d}^2\mathbf{k}'\left[\mathcal{D}_\parallel(\mathbf{k}, \mathbf{k}') + \mathcal{D}_\perp(\mathbf{k}, \mathbf{k}', \omega)\right]\widetilde{\psi}(\mathbf{k}', \omega), \tag{13}$$

where $\check{\alpha}^{-1}(\omega) = \alpha_0^{-1}(\omega) - \mathrm{Re}[\Sigma(\omega)]$. In equation (13), the Fourier transform of the spinor envelope field reads $\widetilde{\psi}(\mathbf{k}, \omega) = [\widetilde{\psi}_A(\mathbf{k}, \omega), \widetilde{\psi}_B(\mathbf{k}, \omega)]^{\mathrm{T}}$, the longitudinal dynamical matrix encoding the Coulomb interactions is given by

$$\mathcal{D}_\parallel(\mathbf{k}, \mathbf{k}') = \begin{bmatrix} \mathcal{D}_\parallel^{AA}(\mathbf{k}, \mathbf{k}') & \mathcal{D}_\parallel^{AB}(\mathbf{k}, \mathbf{k}') \\ \mathcal{D}_\parallel^{AB*}(\mathbf{k}', \mathbf{k}) & \mathcal{D}_\parallel^{BB}(\mathbf{k}, \mathbf{k}') \end{bmatrix}, \tag{14}$$

and the transverse dynamical matrix encoding the photon-mediated interactions reads

$$\mathcal{D}_\perp(\mathbf{k}, \mathbf{k}', \omega) = \begin{bmatrix} \mathcal{D}_\perp^{AA}(\mathbf{k}, \mathbf{k}', \omega) & \mathcal{D}_\perp^{AB}(\mathbf{k}, \mathbf{k}', \omega) \\ \mathcal{D}_\perp^{AB*}(\mathbf{k}', \mathbf{k}, \omega) & \mathcal{D}_\perp^{BB}(\mathbf{k}, \mathbf{k}', \omega) \end{bmatrix}. \tag{15}$$

We will first analyze the longitudinal dynamical matrix elements in equation (14), where the intersublattice (off-diagonal) matrix elements read

$$\mathcal{D}_\parallel^{AB}(\mathbf{k}, \mathbf{k}') = \int\frac{\mathrm{d}^2\mathbf{r}}{(2\pi)^2}\sum_{\mathbf{R}}\mathsf{G}_\parallel(\mathbf{R} - \mathbf{d} + \mathbf{u}(\mathbf{r}) - \mathbf{u}(\mathbf{r} - \mathbf{R} + \mathbf{d})) \\ \times \mathrm{e}^{-\mathrm{i}(\mathbf{K}+\mathbf{k}')\cdot(\mathbf{R}-\mathbf{d})}\mathrm{e}^{\mathrm{i}(\mathbf{k}'-\mathbf{k})\cdot\mathbf{r}}. \tag{16}$$

Since the Coulomb interactions are short-range, the lattice sums converge rapidly in real space. After expanding equation (16) to leading order in the displacement field we obtain

$$\mathcal{D}_\parallel^{AB}(\mathbf{k}, \mathbf{k}') = \int\frac{\mathrm{d}^2\mathbf{r}}{(2\pi)^2}\sum_{\mathbf{R}}\mathsf{G}_\parallel(\mathbf{R} - \mathbf{d})\mathrm{e}^{-\mathrm{i}(\mathbf{K}+\mathbf{k}')\cdot(\mathbf{R}-\mathbf{d})}\mathrm{e}^{\mathrm{i}(\mathbf{k}'-\mathbf{k})\cdot\mathbf{r}} \\ \times \left\{1 - \frac{\beta(\mathbf{R} - \mathbf{d})}{2\pi}\frac{(\mathbf{R}-\mathbf{d})_i}{|\mathbf{R}-\mathbf{d}|^2}\int\mathrm{d}^2\mathbf{q}\,\widetilde{u}_i(\mathbf{q})\left[1 - \mathrm{e}^{-\mathrm{i}\mathbf{q}\cdot(\mathbf{R}-\mathbf{d})}\right]\mathrm{e}^{\mathrm{i}\mathbf{q}\cdot\mathbf{r}}\right\}, \tag{17}$$

where the parameter $\beta(\mathbf{R}) = |\partial \log[\mathsf{G}_\parallel(\mathbf{R})]/\partial \log(|\mathbf{R}|)|$ encodes how the Coulomb interaction strength between dipoles, initially separated by $\mathbf{R}$, changes with respect to small changes in the separation distance, and

$$\widetilde{\mathbf{u}}(\mathbf{q}) = \int \frac{\mathrm{d}^2\mathbf{r}}{2\pi} \mathbf{u}(\mathbf{r}) e^{-i\mathbf{q}\cdot\mathbf{r}} \tag{18}$$

is the Fourier transform of the displacement field. Next, performing the spatial integral in equation (17) we obtain

$$\mathcal{D}_\parallel^{\mathrm{AB}}(\mathbf{k},\mathbf{k}') = \sum_{\mathbf{R}} \mathsf{G}_\parallel(\mathbf{R}-\mathbf{d}) e^{-i(\mathbf{K}+\mathbf{k}')\cdot(\mathbf{R}-\mathbf{d})} \Big\{ \delta(\mathbf{k}'-\mathbf{k}) \\ - \frac{\beta(\mathbf{R}-\mathbf{d})}{2\pi} \frac{(\mathbf{R}-\mathbf{d})_i}{|\mathbf{R}-\mathbf{d}|^2} \widetilde{u}_i(\mathbf{k}-\mathbf{k}') \Big[1 - e^{-i(\mathbf{k}-\mathbf{k}')\cdot(\mathbf{R}-\mathbf{d})} \Big] \Big\}. \tag{19}$$

Finally, expanding equation (19) to leading order in $\mathbf{k}$ and $\mathbf{k}'$ yields

$$\mathcal{D}_\parallel^{\mathrm{AB}}(\mathbf{k},\mathbf{k}') = \sum_{\mathbf{R}} \mathsf{G}_\parallel(\mathbf{R}-\mathbf{d}) e^{-i\mathbf{K}\cdot(\mathbf{R}-\mathbf{d})} \Big\{ \delta(\mathbf{k}'-\mathbf{k}) \big[1 - i(\mathbf{R}-\mathbf{d})_i k_i' \big] \\ - \frac{\beta(\mathbf{R}-\mathbf{d})}{2\pi} \frac{(\mathbf{R}-\mathbf{d})_i(\mathbf{R}-\mathbf{d})_j}{|\mathbf{R}-\mathbf{d}|^2} \widetilde{\nabla} u_{ij}(\mathbf{k}-\mathbf{k}') \Big\}, \tag{20}$$

where we have identified $ik_i\widetilde{u}_j(\mathbf{k}) = \widetilde{\nabla}u_{ij}(\mathbf{k})$, which is the Fourier transform of the displacement gradient tensor defined as $\nabla u_{ij} = \partial u_j/\partial r_i$. Performing similar analysis for the intrasublattice (diagonal) matrix elements in equation (14) we obtain

$$\mathcal{D}_\parallel^{\mathrm{AA/BB}}(\mathbf{k},\mathbf{k}') = \sum_{\mathbf{R}\neq 0} \mathsf{G}_\parallel(\mathbf{R}) e^{-i\mathbf{K}\cdot\mathbf{R}} \Big\{ \delta(\mathbf{k}'-\mathbf{k}) \big[1 - i(\mathbf{R})_i k_i' \big] \\ - \frac{\beta(\mathbf{R})}{2\pi} \frac{(\mathbf{R})_i(\mathbf{R})_j}{|\mathbf{R}|^2} \widetilde{\nabla}u_{ij}(\mathbf{k}-\mathbf{k}') \Big\}. \tag{21}$$

We will now analyze the transverse dynamical matrix elements in equation (15), where the intersublattice (off-diagonal) matrix elements read

$$\mathcal{D}_\perp^{\mathrm{AB}}(\mathbf{k},\mathbf{k}',\omega) = \int \frac{\mathrm{d}^2\mathbf{r}}{(2\pi)^2} \sum_{\mathbf{R}} \mathsf{G}_\perp^{\mathrm{TEM}}(\mathbf{R}-\mathbf{d}+\mathbf{u}(\mathbf{r})-\mathbf{u}(\mathbf{r}-\mathbf{R}+\mathbf{d}),\omega) \\ \times e^{-i(\mathbf{K}+\mathbf{k}')\cdot(\mathbf{R}-\mathbf{d})} e^{i(\mathbf{k}'-\mathbf{k})\cdot\mathbf{r}}. \tag{22}$$

Since the photon-mediated interactions are long-range, we need to perform the lattice sums in reciprocal space where they converge rapidly. To do this, we first insert the inverse Fourier transform of the TEM Green's function (10) into equation (22) which gives

$$\mathcal{D}_\perp^{\mathrm{AB}}(\mathbf{k},\mathbf{k}',\omega) = \int \frac{\mathrm{d}^2\mathbf{r}}{(2\pi)^2} \int \frac{\mathrm{d}^2\mathbf{k}''}{2\pi} \sum_{\mathbf{R}} \widetilde{\mathsf{G}}_\perp^{\mathrm{TEM}}(\mathbf{k}'',\omega) e^{i(\mathbf{k}'-\mathbf{k})\cdot\mathbf{r}} \\ \times e^{i(\mathbf{k}''-\mathbf{k}'-\mathbf{K})\cdot(\mathbf{R}-\mathbf{d})} e^{i\mathbf{k}''\cdot[\mathbf{u}(\mathbf{r})-\mathbf{u}(\mathbf{r}-\mathbf{R}+\mathbf{d})]}, \tag{23}$$

where $\widetilde{\mathsf{G}}_\perp^{\mathrm{TEM}}(\mathbf{k},\omega) = (2a^3 k_\omega^2/L)(k^2 - k_\omega^2)^{-1}$ is the Fourier transform of the TEM Green's function. Next, the expansion of equation (23) to leading order in the displacement field yields

$$\mathcal{D}_\perp^{\mathrm{AB}}(\mathbf{k},\mathbf{k}',\omega) = \int \frac{\mathrm{d}^2\mathbf{r}}{(2\pi)^2} \int \frac{\mathrm{d}^2\mathbf{k}''}{2\pi} \sum_{\mathbf{R}} \widetilde{\mathsf{G}}_\perp^{\mathrm{TEM}}(\mathbf{k}'',\omega) e^{i(\mathbf{k}'-\mathbf{k})\cdot\mathbf{r}} \\ \times e^{i(\mathbf{k}''-\mathbf{k}'-\mathbf{K})\cdot(\mathbf{R}-\mathbf{d})} \Big\{ 1 + \frac{i}{2\pi} k_i'' \int \mathrm{d}^2\mathbf{q}\, \widetilde{u}_i(\mathbf{q}) \big[1 - e^{-i\mathbf{q}\cdot(\mathbf{R}-\mathbf{d})} \big] e^{i\mathbf{q}\cdot\mathbf{r}} \Big\}, \tag{24}$$

and after performing the spatial integral in equation (24) we obtain

$$\mathcal{D}_\perp^{\mathrm{AB}}(\mathbf{k},\mathbf{k}',\omega) = \int \frac{\mathrm{d}^2\mathbf{k}''}{2\pi} \sum_{\mathbf{R}} \widetilde{\mathsf{G}}_\perp^{\mathrm{TEM}}(\mathbf{k}'',\omega) e^{i(\mathbf{k}''-\mathbf{k}'-\mathbf{K})\cdot(\mathbf{R}-\mathbf{d})} \\ \times \Big\{ \delta(\mathbf{k}'-\mathbf{k}) + \frac{i}{2\pi} k_i'' \widetilde{u}_i(\mathbf{k}-\mathbf{k}') \big[1 - e^{-i(\mathbf{k}-\mathbf{k}')\cdot(\mathbf{R}-\mathbf{d})} \big] \Big\}. \tag{25}$$

We now use Poisson's summation identity $\sum_{\mathbf{R}} \exp[i(\mathbf{k}'-\mathbf{k})\cdot\mathbf{R}] = [(2\pi)^2/\mathcal{A}] \sum_{\mathbf{G}} \delta(\mathbf{k}'-\mathbf{k}+\mathbf{G})$, where $\mathcal{A} = 3\sqrt{3}a^2/2$ is the area of the unit cell

in the unstrained lattice, to convert the sum over lattice vectors to a sum over reciprocal lattice vectors

$$\mathcal{D}_\perp^{\mathrm{AB}}(\mathbf{k},\mathbf{k}',\omega) = \frac{2\pi}{\mathcal{A}} \sum_{\mathbf{G}} \phi_{\mathbf{G}} \Big\{ \widetilde{\mathsf{G}}_\perp^{\mathrm{TEM}}(\mathbf{k}'+\mathbf{K}-\mathbf{G},\omega)\delta(\mathbf{k}'-\mathbf{k}) \\ + \frac{i}{2\pi} \Big[\widetilde{\mathsf{G}}_\perp^{\mathrm{TEM}}(\mathbf{k}'+\mathbf{K}-\mathbf{G},\omega)(\mathbf{k}'+\mathbf{K}-\mathbf{G})_i - (\mathbf{k}'\leftrightarrow\mathbf{k}) \Big] \widetilde{u}_i(\mathbf{k}-\mathbf{k}') \Big\}, \tag{26}$$

where $\phi_{\mathbf{G}} = \exp(i\mathbf{G}\cdot\mathbf{d})$ are non-trivial phase factors that are crucial for maintaining the correct symmetry. Finally, expanding equation (26) to leading order in $\mathbf{k}$ and $\mathbf{k}'$ we obtain

$$\mathcal{D}_\perp^{\mathrm{AB}}(\mathbf{k},\mathbf{k}',\omega) = \sum_{\mathbf{G}} \frac{\omega^2\xi^2\phi_{\mathbf{G}}}{\omega_{\mathbf{K}-\mathbf{G}}^2 - \omega^2} \Big\{ \delta(\mathbf{k}'-\mathbf{k}) - \frac{1}{2\pi}\widetilde{\nabla}u_{ii}(\mathbf{k}-\mathbf{k}') \\ - \frac{2c^2(\mathbf{K}-\mathbf{G})_i}{\omega_{\mathbf{K}-\mathbf{G}}^2 - \omega^2} \Big[k_i'\delta(\mathbf{k}'-\mathbf{k}) - \frac{1}{2\pi}(\mathbf{K}-\mathbf{G})_j\widetilde{\nabla}u_{ij}(\mathbf{k}-\mathbf{k}') \Big] \Big\}, \tag{27}$$

where $\xi^2 = 4\pi a^3/\mathcal{A}L$ parameterizes the strength of the light-matter coupling. Performing similar analysis for the intrasublattice (diagonal) matrix elements in equation (15) we obtain

$$\mathcal{D}_\perp^{\mathrm{AA/BB}}(\mathbf{k},\mathbf{k}',\omega) = \sum_{\mathbf{G}} \frac{\omega^2\xi^2}{\omega_{\mathbf{K}-\mathbf{G}}^2 - \omega^2} \Big\{ \delta(\mathbf{k}'-\mathbf{k}) - \frac{1}{2\pi}\widetilde{\nabla}u_{ii}(\mathbf{k}-\mathbf{k}') \\ - \frac{2c^2(\mathbf{K}-\mathbf{G})_i}{\omega_{\mathbf{K}-\mathbf{G}}^2 - \omega^2} \Big[k_i'\delta(\mathbf{k}'-\mathbf{k}) - \frac{1}{2\pi}(\mathbf{K}-\mathbf{G})_j\widetilde{\nabla}u_{ij}(\mathbf{k}-\mathbf{k}') \Big] \Big\} \\ - \mathrm{Re}[\mathsf{G}_\perp^{\mathrm{TEM}}(0,\omega)]\delta(\mathbf{k}'-\mathbf{k}). \tag{28}$$

To obtain an effective Hamiltonian for the polariton envelope fields, we linearize the coupled-dipole equations for simplicity which captures the essential physics away from the light-line. First, we calculate the renormalized resonant frequency ω_{cav} of the dipoles inside the cavity which can be found by solving $\mathrm{Re}[\alpha^{-1}(\omega_{\mathrm{cav}})] = 0$. Next, we evaluate the polarizability correction (5) and the transverse dynamical matrix (15) at the cavity resonant frequency, neglect non-radiative losses, and approximate $\omega_{\mathrm{cav}}^2 - \omega^2 \simeq 2\omega_{\mathrm{cav}}(\omega_{\mathrm{cav}}-\omega)$. Finally, by Fourier transforming equation (13) to the real-space and time domains, we obtain the equation of motion $i\partial_t\psi_{\mathrm{K}}(\mathbf{r},t) = \mathcal{H}_{\mathrm{K}}\psi_{\mathrm{K}}(\mathbf{r},t)$ for the spinor envelope field in the K valley $\psi_{\mathrm{K}}(\mathbf{r},t) = [\psi_{\mathrm{A}}^{\mathrm{K}}(\mathbf{r},t),\psi_{\mathrm{B}}^{\mathrm{K}}(\mathbf{r},t)]^{\mathrm{T}}$, where the effective Hamiltonian is given by equation (3) in the main text. Similarly, we obtain the equation of motion $i\partial_t\psi_{\mathrm{K}'}(\mathbf{r},t) = \mathcal{H}_{\mathrm{K}'}\psi_{\mathrm{K}'}(\mathbf{r},t)$ for the spinor envelope field in the K' valley $\psi_{\mathrm{K}'}(\mathbf{r},t) = [\psi_{\mathrm{A}}^{\mathrm{K}'}(\mathbf{r},t),\psi_{\mathrm{B}}^{\mathrm{K}'}(\mathbf{r},t)]^{\mathrm{T}}$, where the effective Hamiltonian is related to equation (3) by time-reversal symmetry $\mathcal{H}_{\mathrm{K}'} = \mathcal{H}_{\mathrm{K}}^*$, and reads

$$\mathcal{H}_{\mathrm{K}'} = \omega_{\mathrm{D}}(L)\mathbb{1} - iv_{\mathrm{D}}(L)\boldsymbol{\sigma}^*\cdot\nabla + \Phi(\mathbf{r},L)\mathbb{1} + \boldsymbol{\sigma}^*\cdot\mathbf{A}(\mathbf{r},L), \tag{29}$$

where $\boldsymbol{\sigma}^* = [\sigma_x, -\sigma_y]$. Note, since time-reversal symmetry is preserved the pseudo-vector potential couples with opposite signs in the two valleys. In equations (3) and (29) the Dirac frequency reads

$$\omega_{\mathrm{D}}(L) = \omega_{\mathrm{cav}} - \Omega\frac{\omega_0}{\omega_{\mathrm{cav}}} \sum_{\mathbf{R}\neq 0} \mathsf{G}_\parallel(\mathbf{R}) e^{-i\mathbf{K}\cdot\mathbf{R}} \\ + \Omega\frac{\omega_0}{\omega_{\mathrm{cav}}} \mathrm{Re}[\mathsf{G}_\perp^{\mathrm{TEM}}(0,\omega_{\mathrm{cav}})] - \Omega\frac{\omega_0}{\omega_{\mathrm{cav}}} \sum_{\mathbf{G}} \frac{\omega_{\mathrm{cav}}^2\xi^2}{\omega_{\mathbf{K}-\mathbf{G}}^2 - \omega_{\mathrm{cav}}^2}, \tag{30}$$

and the Dirac velocity is given by

$$v_{\mathrm{D}}(L) = -i\Omega\frac{\omega_0}{\omega_{\mathrm{cav}}} \sum_{\mathbf{R}} \mathsf{G}_\parallel(\mathbf{R}-\mathbf{d}) e^{-i\mathbf{K}\cdot(\mathbf{R}-\mathbf{d})} (\mathbf{R}-\mathbf{d})_x \\ - \Omega\frac{\omega_0}{\omega_{\mathrm{cav}}} \sum_{\mathbf{G}} \frac{2\omega_{\mathrm{cav}}^2\xi^2 c^2(\mathbf{K}-\mathbf{G})_x\phi_{\mathbf{G}}}{(\omega_{\mathbf{K}-\mathbf{G}}^2 - \omega_{\mathrm{cav}}^2)^2}. \tag{31}$$

Furthermore, the strain-independent parameter in the pseudo-scalar potential reads

$$\Phi_0(L) = \Omega\frac{\omega_0}{\omega_{\mathrm{cav}}} \sum_{\mathbf{R}\neq 0} \mathsf{G}_\parallel(\mathbf{R}) e^{-i\mathbf{K}\cdot\mathbf{R}} \frac{(\mathbf{R})_x^2}{|\mathbf{R}|^2} \beta(\mathbf{R}) \\ + \Omega\frac{\omega_0}{\omega_{\mathrm{cav}}} \sum_{\mathbf{G}} \Big[\frac{\omega_{\mathrm{cav}}^2\xi^2}{\omega_{\mathbf{K}-\mathbf{G}}^2 - \omega_{\mathrm{cav}}^2} - \frac{2\omega_{\mathrm{cav}}^2\xi^2 c^2(\mathbf{K}-\mathbf{G})_x^2}{(\omega_{\mathbf{K}-\mathbf{G}}^2 - \omega_{\mathrm{cav}}^2)^2} \Big], \tag{32}$$

and the strain-independent parameter in the pseudo-vector potential is given by

$$A_0(L) = \Omega\frac{\omega_0}{\omega_{\mathrm{cav}}} \sum_{\mathbf{R}} \mathsf{G}_\parallel(\mathbf{R}-\mathbf{d}) e^{-i\mathbf{K}\cdot(\mathbf{R}-\mathbf{d})} \frac{(\mathbf{R}-\mathbf{d})_x^2}{|\mathbf{R}-\mathbf{d}|^2} \beta(\mathbf{R}-\mathbf{d}) \\ - \Omega\frac{\omega_0}{\omega_{\mathrm{cav}}} \sum_{\mathbf{G}} \frac{2\omega_{\mathrm{cav}}^2\xi^2 c^2(\mathbf{K}-\mathbf{G})_x^2\phi_{\mathbf{G}}}{(\omega_{\mathbf{K}-\mathbf{G}}^2 - \omega_{\mathrm{cav}}^2)^2}. \tag{33}$$

Note, to evaluate the Dirac frequency (30) one requires a suitable regularization procedure since the last two terms separately diverge (see Supplementary Section 7 for details).

Numerical simulation of polariton wavepackets.— We use the second-order split-operator method [22] to approximate the time evolution of the polariton envelope fields. After a small time δt has elapsed, the polariton envelope field in the K valley is given by

$$\psi_{\mathrm{K}}(\mathbf{r}, t + \delta t) = \mathrm{e}^{-\mathrm{i}\mathcal{H}_{\mathrm{K}}\delta t}\psi_{\mathrm{K}}(\mathbf{r}, t) \,. \tag{34}$$

In the second-order split operator method, the evolution operator in equation (34) is approximated as

$$\mathrm{e}^{-\mathrm{i}\mathcal{H}_{\mathrm{K}}\delta t} = \mathrm{e}^{-\frac{\mathrm{i}}{2}\mathcal{H}_{\mathrm{K}}^{\varepsilon}\delta t}\mathrm{e}^{-\mathrm{i}\mathcal{H}_{\mathrm{K}}^{0}\delta t}\mathrm{e}^{-\frac{\mathrm{i}}{2}\mathcal{H}_{\mathrm{K}}^{\varepsilon}\delta t} + \mathcal{O}(\delta t^3) \,, \tag{35}$$

where $\mathcal{H}_{\mathrm{K}}^{0} = \omega_{\mathrm{D}}\mathbb{1} + \mathrm{i}v_{\mathrm{D}}\boldsymbol{\sigma}\cdot\nabla$ and $\mathcal{H}_{\mathrm{K}}^{\varepsilon} = \Phi(\mathbf{r})\mathbb{1} + \boldsymbol{\sigma}\cdot\mathbf{A}(\mathbf{r})$. Note, the cubic error in δt is due to the noncommutativity of the position and gradient operators. To calculate the field after time $N_t\delta t$ has elapsed, we have to apply the operation (35) iteratively

$$\psi_{\mathrm{K}}(\mathbf{r}, t + N_t\delta t) \approx \prod_{i=1}^{N_t}\left(\mathcal{M}_r^{\mathrm{K}}\mathcal{F}^{-1}\mathcal{M}_k^{\mathrm{K}}\mathcal{F}\mathcal{M}_r^{\mathrm{K}}\right)\psi_{\mathrm{K}}(\mathbf{r}, t) \,, \tag{36}$$

where $\mathcal{F}$ and $\mathcal{F}^{-1}$ represent the direct and inverse Fourier transform operations, respectively. Using the standard identity for the exponential of Pauli matrices, we can write the position-dependent operator in equation (36) as

$$\mathcal{M}_r^{\mathrm{K}} = \mathrm{e}^{-\mathrm{i}\delta t\Phi/2}\left[\cos(\delta t A/2)\mathbb{1} - \mathrm{i}\frac{\sin(\delta t A/2)}{A}\boldsymbol{\sigma}\cdot\mathbf{A}\right] \,, \tag{37}$$

and the momentum-dependent operator as

$$\mathcal{M}_k^{\mathrm{K}} = \mathrm{e}^{-\mathrm{i}\omega_{\mathrm{D}}\delta t}\left[\cos(v_{\mathrm{D}}k\delta t)\mathbb{1} + \mathrm{i}\frac{\sin(v_{\mathrm{D}}k\delta t)}{k}\boldsymbol{\sigma}\cdot\mathbf{k}\right] \,. \tag{38}$$

Similarly, the evolution of the polariton envelope field in the K′ valley can be approximated as

$$\psi_{\mathrm{K}'}(\mathbf{r}, t + N_t\delta t) \approx \prod_{i=1}^{N_t}\left(\mathcal{M}_r^{\mathrm{K}'}\mathcal{F}^{-1}\mathcal{M}_k^{\mathrm{K}'}\mathcal{F}\mathcal{M}_r^{\mathrm{K}'}\right)\psi_{\mathrm{K}'}(\mathbf{r}, t) \,, \tag{39}$$

where the operators $\mathcal{M}_r^{\mathrm{K}'}$ and $\mathcal{M}_k^{\mathrm{K}'}$ are related to equations (37) and (38) by the replacement $\boldsymbol{\sigma} \leftrightarrow \boldsymbol{\sigma}^*$ and $\mathbf{k} \leftrightarrow -\mathbf{k}$.

For the simulations in figure 3c, we initialize the following Gaussian wavepackets

$$\psi_{\mathrm{K}}(\mathbf{r}, t = 0) = \frac{1}{2w\sqrt{2\pi}}\mathrm{e}^{-\frac{|\mathbf{r}|^2}{2w^2}}\begin{bmatrix}1 \\ -\,\mathrm{sgn}(v_{\mathrm{D}})\end{bmatrix}\mathrm{e}^{\mathrm{i}\mathbf{k}_{\mathrm{in}}\cdot\mathbf{r}} \,, \tag{40}$$

and

$$\psi_{\mathrm{K}'}(\mathbf{r}, t = 0) = \frac{1}{2w\sqrt{2\pi}}\mathrm{e}^{-\frac{|\mathbf{r}|^2}{2w^2}}\begin{bmatrix}1 \\ \mathrm{sgn}(v_{\mathrm{D}})\end{bmatrix}\mathrm{e}^{\mathrm{i}\mathbf{k}_{\mathrm{in}}\cdot\mathbf{r}} \,, \tag{41}$$

in the K and K′ valleys, respectively. We consider wavepackets that are located in the lower polariton band with a fixed central frequency $\delta\omega = -0.001\omega_0$ relative to the Dirac point, and an initial central wavevector $\mathbf{k}_{\mathrm{in}} = -|\delta\omega/v_{\mathrm{D}}|\hat{\mathbf{x}}$. Furthermore, the wavepackets are initially centred at the origin with a width of $w = 100a$. We then track the centre-of-mass trajectory of the wavepackets for the two valleys which is given by

$$\langle\mathbf{r}\rangle_{\mathrm{K}/\mathrm{K}'} = \frac{\int \mathrm{d}^2\mathbf{r}\,|\psi_{\mathrm{K}/\mathrm{K}'}|^2\mathbf{r}}{\int \mathrm{d}^2\mathbf{r}\,|\psi_{\mathrm{K}/\mathrm{K}'}|^2} \,. \tag{42}$$

In Supplementary Section 2 we go beyond the linear Dirac cone approximation by including second order field gradients in the effective Hamiltonian.

Effective polarizability and local spectral function.— To describe a resonant dipole's response to a local driving field, one has to take into account the strong multiple scattering within the metasurface. Therefore, we define the effective polarizability of a dipole located at $\mathbf{r}_0$ to be

$$\alpha_{\mathrm{eff}}^{-1}(\omega) = \alpha^{-1}(\omega) - \mathsf{S}(\mathbf{r}_0, \mathbf{r}_0, \omega) \,, \tag{43}$$

where the scattering function

$$\mathsf{S}(\mathbf{r}_0, \mathbf{r}_0, \omega) = \sum_{\mu=1}^{N}\sum_{\nu=1}^{N}\mathsf{G}(\mathbf{r}_0 - \mathbf{r}_\mu, \omega)[\mathcal{T}^{(N)}(\omega)]_{\mu\nu}\mathsf{G}(\mathbf{r}_\nu - \mathbf{r}_0, \omega) \tag{44}$$

encodes all the multiple-scattering events between the other N dipoles in the metasurface located at positions $\mathbf{r}_1, \ldots, \mathbf{r}_N$. In equation (44), $\mathcal{T}^{(N)}(\omega)$ is the T-matrix with matrix elements

$$[\mathcal{T}^{(N)}(\omega)]_{\mu\nu} = \alpha(\omega)[\mathcal{W}^{-1}(\omega)]_{\mu\nu} \,, \tag{45}$$

where the matrix elements of $\mathcal{W}(\omega)$ read

$$[\mathcal{W}(\omega)]_{\mu\nu} = \delta_{\mu\nu} - (1 - \delta_{\mu\nu})\mathsf{G}(\mathbf{r}_\mu - \mathbf{r}_\nu, \omega)\alpha(\omega) \,. \tag{46}$$

Note, here we include the full cavity Green's function given by equation (8) and we keep the frequency dependence. In figures 4c-e, we plot the local spectral function $\mathrm{Im}[\alpha_{\mathrm{eff}}(\omega)]$ for the resonant dipole located at $\mathbf{r}_0 = [0, a/2]$ on the B sublattice within a metasurface consisting of approximately 14,000 dipoles and arranged in a circular configuration (before the applied strain).

Author contributions

C.-R.M. conceived the idea, developed the theory, performed the calculations, and wrote the manuscript; S.A.R.H. contributed to the theoretical understanding; E.M. initiated the study, contributed to the theoretical understanding, and supervised the project; All authors commented on the manuscript.

Data availability

All relevant data are available from the corresponding authors upon reasonable request.

Competing interests

The authors declare no competing interests.

Additional information

Correspondence and requests for materials should be addressed to C.-R.M or E.M.